

Joint contrast source inversion of marine magnetotelluric and controlled-source electromagnetic data

Torgeir Wiik¹, Ketil Hokstad², Bjørn Ursin³, and Lutz Mütschard³

ABSTRACT

We evaluated a joint contrast source inversion scheme for marine controlled-source electromagnetic (mCSEM) and magnetotelluric (MT) data based on a scattered field formulation. The scheme considered only contrasts in electric conductivity, and it allowed the medium to be transversely isotropic with a vertical symmetry axis. The method was based on the integral equation formulation of electromagnetic field propagation, and we demonstrated how the method solved the inverse problem of determining the conductivity structure of the subsurface. The method did not consider MT impedances as data input to inversion, but instead explicitly the field components, and the consequences of this approach, were discussed. Although there are challenges associated with source estimation and data noise, we found it easier to make

connections to CSEM and it simplified some computational issues. Three synthetic examples were considered to demonstrate the method: a reservoir below an anisotropic overburden, a salt diapir, and a reservoir near a salt diapir. MT and CSEM data were first treated sequentially, first inverting the MT data and using the result as the initial model and in the regularization in CSEM inversion. The result of this approach was then compared to a joint inversion. The same approach was finally applied to a real data set. We found that sequential inversions in some situations produced similar results as joint inversions, and hence, joint inversion may not be necessary in all situations. Nonetheless, joint inversion could be useful for imaging salt diapirs and eventually hydrocarbons near salt. In particular, it was useful to map the spatial extent of the salt diapirs. It was, moreover, a useful tool for checking data consistency in different models with respect to several data types.

INTRODUCTION

Marine controlled-source electromagnetic (mCSEM) and magnetotelluric (MT) prospecting are closely linked by both being electromagnetic methods sensitive to the same physical parameter — electric conductivity. However, with regard to sensitivity, the two methods are inherently different. The use of mCSEM data in hydrocarbon prospecting is based on the assumption that hydrocarbon-saturated formations possess a significantly lower electric conductivity compared to their surroundings. The EM field emitted from a controlled source traveling inside this resistive region will be less attenuated at far source/receiver offsets than the field propagating in water-saturated formations, and the effect of such resistive areas should thus be recognizable at far offsets (see e.g., [Eidesmo et al., 2002](#)). The source in mCSEM is usually a horizontal electric

dipole emitting transverse electric and transverse magnetic polarized electromagnetic fields in the frequency range of 0.1–10 Hz.

The MT assumption, however, is a vertically incident plane wave caused by variations in the earth's magnetosphere, thus inducing mainly horizontal currents in the subsurface. The MT frequency content usually starts below that of mCSEM but has a larger bandwidth, and the MT signal thus penetrates deeper into the subsurface and contains information regarding more large-scale structures and trends. The frequency content in marine MT varies with water depth because the conductive water column acts as a low-pass filter with decreasing cut-off with increasing depth. A good overview of the MT method can be found in [Simpson and Bahr \(2005\)](#).

In contrast to mCSEM, the MT method is not as sensitive to laterally elongated, thin resistive reservoirs because it sets up mainly horizontal currents traveling in the high-conductivity structures of

Manuscript received by the Editor 12 November 2012; revised manuscript received 30 April 2013; published online 17 October 2013.

¹Formerly Norwegian University of Science and Technology, Department for Petroleum Engineering and Applied Geophysics, Trondheim, Norway; presently Statoil Research Center, Ranheim, Norway. E-mail: torgeir.wiik@ntnu.no.

²Statoil Research Center, Ranheim, Norway. E-mail: kehok@statoil.com.

³Norwegian University of Science and Technology, Department for Petroleum Engineering and Applied Geophysics, Trondheim, Norway. E-mail: bjorn.ursin@ntnu.no; lutz.mutschard@ntnu.no.

© 2013 Society of Exploration Geophysicists. All rights reserved.

the subsurface. Thus, the MT signal does not couple into thin, resistive anomalies. Because of this, and the difference in frequency content, MT data are nowadays typically used in hydrocarbon exploration to image background trends before performing mCSEM inversion and to image large structures such as salt diapirs (Hokstad et al., 2011; Ceci et al., 2012) and subbasalt structures (Heincke et al., 2006; Jegen et al., 2009; Colombo et al., 2011). Further, by inducing predominantly horizontal currents, MT data contain information regarding the horizontal conductivity in the subsurface. This information, in combination with mCSEM data, is useful for anisotropic inversion of electromagnetic data. We note that although MT is not very sensitive to thin resistive layers, the use of the ratio of horizontal and vertical magnetic field components, called “tipper,” has been investigated and patented for hydrocarbon detection (Fox and Ingerov, 2007).

A lot of work has been performed within EM inverse scattering (see Colton and Kress [1992] for a theoretical overview). In particular, solving the inverse scattering problem to estimate the subsurface conductivity structure has become increasingly important in exploration geophysics. Traditionally, mCSEM and MT data have been treated separately; see, for instance, Constable et al. (1987), Newman and Hoversten (2000), Rodi and Mackie (2001), Zhdanov (2002), Abubakar et al. (2008a), Plessix and Mulder (2008), Zhdanov et al. (2009), Newman et al. (2010), and Wiik et al. (2011) for a variety of methods. However, lately more attention has been given to treating these two data types simultaneously in joint inversion schemes (Mackie et al., 2007; Abubakar et al., 2009; Commer and Newman, 2009; Price and Watts, 2009; Sasaki, 2013). Joint inversion is attractive because it makes the inversion more data controlled with less human intervention, and it introduces more data points into the inversion. The mCSEM and MT methods link in naturally with each other because the unknown parameters are the same, but they emphasize different elements of the conductivity tensor. This suggests that reliable joint inversion results should be obtained. The mentioned articles consider isotropic models, and mostly compare stand-alone mCSEM and MT results to the results obtained by joint inversion. We consider TIV (transversely isotropic in the vertical direction) anisotropic inversion and compare joint inversion results to those obtained by an individual MT inversion and an individual mCSEM inversion using the MT inversion result as initial model and reference model in the regularization. This comparison is done to investigate whether joint inversion gives a different result than a sequential approach where information from earlier inversions is used.

We apply the so-called 3D contrast source inversion (CSI) method based on integral equations to joint mCSEM and MT inversion. The method was applied to mCSEM data by Wiik et al. (2011), but it has also been applied to different problems, for instance, biomedical imaging (Abubakar et al., 2002). See Abubakar and van den Berg (2004) for a thorough introduction to the method. The CSI method approximates the associated nonlinear optimization problem by alternately approximating the solution to two linear problems. Further, if the background model, where the Green’s tensors are computed, has one or more invariant directions and the perturbation from the background model has a small spatial extent, this approach becomes efficient both with respect to computational time and memory. This splitting approach is fundamentally different from the inversion papers cited in the previous paragraph, which consider conventional Gauss-Newton methods or gradient-based

methods. In addition, our method differs from traditional MT inversion methods because it is based directly on the field components and not impedances. This choice was made for several reasons. First, because Maxwell’s equations are formulated in field components, it is, in many situations, more intuitive to use these. It also provides a more direct bridge for comparing and using methodology from other fields in electromagnetism where field components are used. Specifically, it allows using mCSEM software on MT problems with only minor modifications. Second, the field components are closer to the actual measurements, electric field potential, and induced currents, because only a Fourier transform is applied to the recorded time series. From the recorded time series, the electric and magnetic fields in the frequency domain are deduced, whereas the impedance tensor is a combination of the field components again. Third, from an optimization point of view, the construction of the Jacobi matrix needed in Gauss-Newton schemes is simpler because the impedances are nonlinear functionals of the field components. Finally, we note that because we are doing linearized inversions, we would like our modeling operator to behave as linearly as possible. The linearization of the MT impedance modeling operator is a nonlinear combination of nonlinear field component modeling operators, and thus it is natural to question the quality of the linearized impedance operator compared to the linearized field component operator. However, the approach is of course also hampered with some drawbacks. The most severe is the need to estimate the source field. In this paper, this was performed by using an approximate 1D reference receiver, where an approximate model was known from previous work. This simplifies the estimation because the field separates into two independent modes under the vertically incident plane wave assumption. Further, it is important that the data are calculated from a time window common for all receivers. Because the response is dependent on the source signature when using field components, it is important that all receivers measure the response from the same effective source field. The raw recorded time series are also contaminated by quite high noise levels. To obtain impedances with sufficiently low noise levels, processing of MT impedances usually include several steps to reduce noise, for instance, remote referencing and robust processing. Strategies to reduce the noise levels when treating the MT data on field component form to improve the data quality are desirable and need to be developed in the future. In our field data example, only stacking signals over time windows existing at all receivers was used to reduce the noise level.

In this paper, we apply the CSI algorithm to the low-frequency diffusive fields in mCSEM and MT for joint inversion. The MT data are represented as field components, rather than impedances, and we study the properties of this joint inversion using synthetic and real examples. We use the integral equation framework described earlier by, e.g., Wannamaker et al. (1984), de Hoop (1995), Zhdanov (2002), and Abubakar and van den Berg (2004), but the CSI method has also been explored using finite differences (Abubakar et al., 2008b). The method introduces so-called contrast sources, which appear due to a conductivity contrast, or relative difference, compared to a chosen background. The contrast sources can be interpreted as sources emitting the scattered signal from an anomalous object. The CSI method is thus equivalent to inverting for anomalous currents due to the conductivity contrast. Based on these contrast sources, we alternately minimize a cost functional with respect to the contrast sources and the contrast between the real medium and a chosen background medium,

respectively. The final goal is to obtain an estimate of the contrast that describes the difference between the chosen background and the estimated medium. Thus, the contrast sources are only needed as intermediate variables.

Inverse problems are often ill posed in the Hadamard sense (McOwen, 1996). This means that the problem might not depend continuously on the initial conditions and that there exists several solutions. This is true for the electromagnetic inverse problem of estimating the subsurface conductivity (Zhdanov, 2002), and hence there is a need for regularization to constrain the problem. Regularization is a wide term and may be introduced in several ways, for instance, multiplicatively into the cost functional as described by Abubakar and van den Berg (2004), or linearly (Tikhonov and Arsenin, 1977). We will introduce here a regularizer linearly into the cost functional, which enforces the contrast estimate to remain close to a reference model in some sense, described by weights.

We first apply the CSI method to three synthetic examples to study some properties of joint mCSEM and MT inversion. First, we consider a model with a reservoir below an anisotropic layer in the overburden. This is a setting that often arises in hydrocarbon exploration, and we compare the result of sequential MT and mCSEM inversions to a joint inversion. In the second example, we consider a salt diapir model, while the third example treats the difficult situation of locating a reservoir near a large salt structure. The last two examples are similar to the setting in our real data example that we present at the end and whose data are acquired over a salt diapir.

THEORY

Forward scattering

The theory in this section was explained similarly by Wiik et al. (2011) but is included here for the sake of completeness. It is well known that the electric and magnetic field vectors \mathbf{e} and \mathbf{h} in the frequency domain satisfy

$$\nabla \times \mathbf{e} = i\omega\mu_0\mathbf{h} \quad (1)$$

and

$$\nabla \times \mathbf{h} = \tilde{\sigma}_0\mathbf{e} + \mathbf{j}^s \quad (2)$$

when accepting Ohm's law for conduction currents

$$\mathbf{j} = \sigma\mathbf{e}. \quad (3)$$

Here, \mathbf{j}^s is the electric source current, $i = \sqrt{-1}$, ω is the angular frequency, $\mu_0 = \mu_0\mathbf{I}$ is the magnetic permeability, and $\tilde{\sigma}_0 = \sigma_0 - i\omega\epsilon_0\mathbf{I}$ is the complex electric conductivity. We have let \mathbf{I} denote the identity tensor, ϵ_0 is the electric permittivity, and we consider a TIV medium with electric conductivity given by the tensor

$$\sigma_0 = \begin{pmatrix} \sigma_{0,h} & 0 & 0 \\ 0 & \sigma_{0,h} & 0 \\ 0 & 0 & \sigma_{0,v} \end{pmatrix} = \sigma_{0,v} \begin{pmatrix} \Upsilon & 0 & 0 \\ 0 & \Upsilon & 0 \\ 0 & 0 & 1 \end{pmatrix}. \quad (4)$$

Further, $\sigma_{0,h}$ and $\sigma_{0,v}$ denote the vertical and horizontal conductivities, which may differ in a TIV anisotropic medium, and $\Upsilon = \sigma_h/\sigma_v$ denotes the anisotropy ratio, which describes the degree of anisotropy in the medium, given for arbitrary conductivities. Anisotropy at the mCSEM and MT scale can arise as a consequence of a specific grain layering (Negi and Saraf, 1989) or thin layering (Newman et al., 2010), and it is essential to include in electromagnetic hydrocarbon prospecting. These parameters are assumed to have some spatial dependence.

Central in the theory of integral equations is the impulse response, or Green's functions. Green's tensors generalize the concept of Green's functions for scalar equations to vector-valued equations (Green, 1828; McOwen, 1996), and they represent fields from a point source with different polarizations. The Green's tensors in three dimensions are thus represented by 3×3 matrices, with element (i,j) representing the field in the i -direction from a point source polarized in the j -direction, $i, j \in \{x, y, z\}$. Thus, they satisfy

$$\nabla \times \mathbf{G}^E(\mathbf{x}, \mathbf{x}_0) = i\omega\mu_0\mathbf{G}^H(\mathbf{x}, \mathbf{x}_0), \quad (5)$$

$$\nabla \times \mathbf{G}^H(\mathbf{x}, \mathbf{x}_0) = \tilde{\sigma}_0\mathbf{G}^E(\mathbf{x}, \mathbf{x}_0) + \mathbf{I}\delta(\mathbf{x} - \mathbf{x}_0), \quad (6)$$

where \mathbf{G}^E and \mathbf{G}^H : are the electric and magnetic Green's tensors, respectively, δ : is Dirac's delta function and \mathbf{x}_0 : is the source position.

We may then express the solution to equations 1 and 2 for an electric source with current signature \mathbf{j}^s by (Zhdanov, 2002)

$$e_i(\mathbf{x}) = \int_{\mathbb{R}^3} G_{ij}^E(\mathbf{x}, \mathbf{x}') j_j^s(\mathbf{x}') d\mathbf{x}', \quad (7)$$

$$h_i(\mathbf{x}) = \int_{\mathbb{R}^3} G_{ij}^H(\mathbf{x}, \mathbf{x}') j_j^s(\mathbf{x}') d\mathbf{x}', \quad (8)$$

where we have used Einstein's convention of sums and $i, j \in \{x, y, z\}$ denotes the components of the vectors and tensors. Equations 7 and 8 represent the formal solution to Maxwell's equations due to a known electric source in terms of Green's tensors.

Let us now consider the situation illustrated by Figure 1: A background model \mathcal{B} is described by the parameters σ_0 , ϵ_0 , and μ_0 , and we assume that there is a finite domain \mathcal{D} in \mathcal{B} that contains an anomaly compared to the electric conductivity of the background model. In our setting, the inhomogeneity in \mathcal{D} might represent a hydrocarbon reservoir or a salt diapir. We then illuminate \mathcal{D} by an electric field from the outside, and we record the response of the scattering at receivers on a domain \mathcal{S} outside \mathcal{D} . The incident electric and magnetic field e_i^{inc} and h_i^{inc} in \mathcal{D} due to an electric source is now given by equations 7 and 8. The incident fields contain the entire response of the background model \mathcal{B} .

Let the conductivity inside \mathcal{D} be denoted by σ . Then, the electric field inside \mathcal{D} satisfies (Hohmann, 1987)

$$e_i(\mathbf{x}) = e_i^{\text{inc}}(\mathbf{x}) + \int_{\mathcal{D}} G_{ij}^E(\mathbf{x}, \mathbf{x}') \sigma_{0,v}(\mathbf{x}') \chi_{jj}(\mathbf{x}') e_j(\mathbf{x}') d\mathbf{x}', \\ \mathbf{x} \in \mathcal{D}. \quad (9)$$

Equation 9 is known as the scattering equation because it relates the incident field with the total field via the contrast that causes scattering. The contrast χ is given by

$$\chi = \begin{pmatrix} \chi_h & 0 & 0 \\ 0 & \chi_h & 0 \\ 0 & 0 & \chi_v \end{pmatrix} = \begin{pmatrix} \frac{\sigma_h}{\sigma_{0,v}} - \frac{\sigma_{0,h}}{\sigma_{0,v}} & 0 & 0 \\ 0 & \frac{\sigma_h}{\sigma_{0,v}} - \frac{\sigma_{0,h}}{\sigma_{0,v}} & 0 \\ 0 & 0 & \frac{\sigma_v}{\sigma_{0,v}} - 1 \end{pmatrix}. \quad (10)$$

Upon establishing the total electric field inside \mathcal{D} , it is straightforward to calculate the scattered field at receiver locations by (Hohmann, 1987)

$$f_i^E(\mathbf{x}) = \int_{\mathcal{D}} G_{ij}^E(\mathbf{x}, \mathbf{x}') \sigma_{0,v}(\mathbf{x}') \chi_{jj}(\mathbf{x}') e_j(\mathbf{x}') d\mathbf{x}', \quad \mathbf{x} \in \mathcal{S}, \quad (11)$$

$$f_i^H(\mathbf{x}) = \int_{\mathcal{D}} G_{ij}^H(\mathbf{x}, \mathbf{x}') \sigma_{0,v}(\mathbf{x}') \chi_{jj}(\mathbf{x}') e_j(\mathbf{x}') d\mathbf{x}', \quad \mathbf{x} \in \mathcal{S}. \quad (12)$$

Hence, given the Green's tensors of the background medium, we can calculate the response at \mathcal{S} due to the inhomogeneity using equations 9–12. For a more thorough overview of the theory related to the integral equation framework for geophysical applications, refer to Zhdanov (2002).

To simplify the notation, we introduce the vectors $\mathbf{e} = (e_x, e_y, e_z)^T$, $\mathbf{f}^E = (f_x^E, f_y^E, f_z^E)^T$, and $\mathbf{f}^H = (f_x^H, f_y^H, f_z^H)^T$ and rewrite equations 9–12 in terms of operators as

$$\mathbf{e} = \mathbf{e}^{\text{inc}} + G^{E,\mathcal{D}} \chi \mathbf{e}, \quad (13)$$

$$\mathbf{f}^E = G^{E,\mathcal{S}} \chi \mathbf{e}, \quad (14)$$

$$\mathbf{f}^H = G^{H,\mathcal{S}} \chi \mathbf{e}, \quad (15)$$

where $G^{E,\mathcal{D}}$, $G^{E,\mathcal{S}}$, and $G^{H,\mathcal{S}}$ denote integral operators.

Contrast source inversion

This section describes how the CSI method is applied to the problem of estimating χ inside \mathcal{D} given both the mCSEM and MT scattered fields. This method is an extension of the method presented in Wiik et al. (2011), which only dealt with mCSEM data. The method is directly applicable to synthetic MT inversion because the incident plane wave is then known, but it differs from the conventional MT inversion methods, which are usually based on fitting impedances to be independent of properties such as the polarization and strength of the incident plane wave. In the next section, we suggest a possible solution to overcome the issue of source estimation for real data.

To this end, we introduce sets of mCSEM and MT contrast sources defined as

$$\mathcal{W}_{\text{mCSEM}} = \{\mathbf{w}_{\text{mCSEM}}^{j,k}\}_{j=1 \dots N_s}^{k=1 \dots N_{f_{\text{mCSEM}}}} = \{\chi \mathbf{e}_{\text{mCSEM}}^{j,k}\}_{j=1 \dots N_s}^{k=1 \dots N_{f_{\text{mCSEM}}}}, \quad (16)$$

$$\mathcal{W}_{\text{MT}} = \{\mathbf{w}_{\text{MT}}^k\}_{k=1 \dots N_{f_{\text{MT}}}} = \{\chi \mathbf{e}_{\text{MT}}^k\}_{k=1 \dots N_{f_{\text{MT}}}}, \quad (17)$$

where N_s is the total number of mCSEM source positions and $N_{f_{\text{mCSEM/MT}}}$ is the number of mCSEM and MT frequencies, respectively. Introducing this into equations 13–15 yields for a given source and frequency, and for both data types

$$\mathbf{e} = \mathbf{e}^{\text{inc}} + G^{E,\mathcal{D}} \mathbf{w}, \quad (18)$$

$$\mathbf{f}^E = G^{E,\mathcal{S}} \mathbf{w}, \quad (19)$$

$$\mathbf{f}^H = G^{H,\mathcal{S}} \mathbf{w}. \quad (20)$$

We will from now on use a norm similar to that associated with $L^2(A)$, where $A \subset \mathbb{R}^3$ is some domain, which is given by

$$\|f\|_A^2 = \int_A |f(\mathbf{x})|^2 d\mathbf{x}. \quad (21)$$

For more information on the norms, refer to Abubakar and van den Berg (2004).

We define the joint CSI problem as a minimization problem as follows:

Find the contrast χ , the set of mCSEM contrast sources $\mathcal{W}_{\text{mCSEM}} = \{\mathbf{w}_{\text{mCSEM}}^{j,k}\}_{j=1 \dots N_s}^{k=1 \dots N_{f_{\text{mCSEM}}}}$, and the set of MT contrast sources $\mathcal{W}_{\text{MT}} = \{\mathbf{w}_{\text{MT}}^k\}_{k=1 \dots N_{f_{\text{MT}}}}$, such that the cost functional

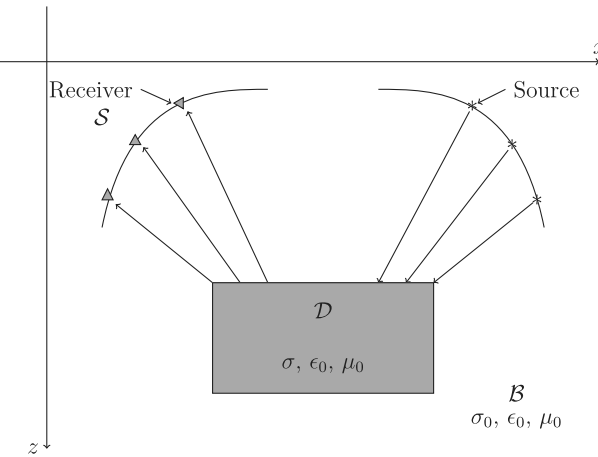


Figure 1. Schematic cross section of the model.

$$\begin{aligned}
F_1(\mathcal{W}_{\text{mCSEM}}, \mathcal{W}_{\text{MT}}, \boldsymbol{\chi}) \\
= & \alpha_{1,\text{mCSEM}}^E \sum_{k=1}^{N_{\text{f}_{\text{mCSEM}}}} \sum_{j=1}^{N_s} \|\Xi_{\text{mCSEM}}^{E,j,k} (\mathbf{f}_{\text{mCSEM}}^{E,j,k} - G^{E,S,k} \mathbf{W}_{\text{mCSEM}}^{j,k})\|_{\mathcal{S}}^2 \\
& + \alpha_{1,\text{mCSEM}}^H \sum_{k=1}^{N_{\text{f}_{\text{mCSEM}}}} \sum_{j=1}^{N_s} \|\Xi_{\text{mCSEM}}^{H,j,k} (\mathbf{f}_{\text{mCSEM}}^{H,j,k} - G^{H,S,k} \mathbf{W}_{\text{mCSEM}}^{j,k})\|_{\mathcal{S}}^2 \\
& + \alpha_{2,\text{mCSEM}} \sum_{k=1}^{N_{\text{f}_{\text{mCSEM}}}} \sum_{j=1}^{N_s} \|\boldsymbol{\chi} \mathbf{e}_{\text{mCSEM}}^{\text{inc},j,k} - \mathbf{W}_{\text{mCSEM}}^{j,k} + \boldsymbol{\chi}^{G^{E,D,k}} \mathbf{W}_{\text{mCSEM}}^{j,k}\|_{\mathcal{D}}^2 \\
& + \alpha_{1,\text{MT}}^E \sum_{k=1}^{N_f} \|\Xi_{\text{MT}}^{E,k} (\mathbf{f}_{\text{MT}}^{E,k} - G^{E,S,k} \mathbf{W}_{\text{MT}}^k)\|_{\mathcal{S}}^2 \\
& + \alpha_{1,\text{MT}}^H \sum_{k=1}^{N_f} \|\Xi_{\text{MT}}^{H,k} (\mathbf{f}_{\text{MT}}^{H,k} - G^{H,S,k} \mathbf{W}_{\text{MT}}^k)\|_{\mathcal{S}}^2 \\
& + \alpha_{2,\text{MT}} \sum_{k=1}^{N_f} \|\boldsymbol{\chi} \mathbf{e}_{\text{MT}}^{\text{inc},k} - \mathbf{W}_{\text{MT}}^k + \boldsymbol{\chi}^{G^{E,D,k}} \mathbf{W}_{\text{MT}}^k\|_{\mathcal{D}}^2
\end{aligned} \tag{22}$$

is minimized.

Here, the first, second, fourth, and fifth terms are the associated data fit; i.e., the modeled data should fit the measured data for the different fields and data types, respectively. The third and sixth terms are associated with solving equation 18. These two terms may be viewed as a physical regularization enforcing a consistent coupling between the contrast sources and the contrast in the scattering domain (Abubakar and van den Berg, 2004). Here, $\alpha_{1,\text{mCSEM}}^E$, $\alpha_{1,\text{mCSEM}}^H$, and $\alpha_{2,\text{mCSEM}}$ are normalization factors given by

$$\alpha_{1,\text{mCSEM}}^{E-1} = \sum_{k=1}^{N_{\text{f}_{\text{mCSEM}}}} \sum_{j=1}^{N_s} \|\Xi_{\text{mCSEM}}^{E,j,k} \mathbf{f}_{\text{mCSEM}}^{E,j,k}\|_{\mathcal{S}}^2, \tag{23}$$

$$\alpha_{1,\text{mCSEM}}^{H-1} = \sum_{k=1}^{N_{\text{f}_{\text{mCSEM}}}} \sum_{j=1}^{N_s} \|\Xi_{\text{mCSEM}}^{H,j,k} \mathbf{f}_{\text{mCSEM}}^{H,j,k}\|_{\mathcal{S}}^2, \tag{24}$$

$$\alpha_{2,\text{mCSEM}}^{-1} = \sum_{k=1}^{N_{\text{f}_{\text{mCSEM}}}} \sum_{j=1}^{N_s} \|\boldsymbol{\chi} \mathbf{e}_{\text{mCSEM}}^{\text{inc},j,k}\|_{\mathcal{D}}^2, \tag{25}$$

and $\alpha_{1,\text{MT}}^E$, $\alpha_{1,\text{MT}}^H$, and $\alpha_{2,\text{MT}}$ are given by

$$\alpha_{1,\text{MT}}^{E-1} = \sum_{k=1}^{N_f} \|\Xi_{\text{MT}}^{E,k} \mathbf{f}_{\text{MT}}^{E,k}\|_{\mathcal{S}}^2, \tag{26}$$

$$\alpha_{1,\text{MT}}^{H-1} = \sum_{k=1}^{N_f} \|\Xi_{\text{MT}}^{H,k} \mathbf{f}_{\text{MT}}^{H,k}\|_{\mathcal{S}}^2, \tag{27}$$

$$\alpha_{2,\text{MT}}^{-1} = \sum_{k=1}^{N_f} \|\boldsymbol{\chi} \mathbf{e}_{\text{MT}}^{\text{inc},k}\|_{\mathcal{D}}^2. \tag{28}$$

The symbol Ξ denotes the data weights.

We solve the CSI according to the algorithm that Abubakar and van den Berg (2004) and Abubakar et al. (2004) present, and we use the iterative, alternating scheme shown in Algorithm 1, which approximates the full nonlinear problem by two linear problems:

Algorithm 1. Pseudocode for the implementation of the inversion scheme.

Input: Initial contrast and contrast sources

foreach iteration **do**

foreach mCSEM frequency **do**

foreach source **do**

Minimize equation 22 with respect to $\mathbf{w}_{\text{mCSEM}}^{j,k}$

end

end

foreach MT frequency **do**

Minimize equation 22 with respect to \mathbf{w}_{MT}^k

end

Minimize equation 22 with respect to $\boldsymbol{\chi}$

if stop criterion is true **then**

stop iterations

else

proceed to next iteration

end

end

The iterations are stopped if the relative difference between the values of the cost functional at two subsequent iterations is below a user specified threshold. An example of the computational resources required is given in Wiik et al. (2011).

Due to the ill posedness of the electromagnetic inverse problem (Zhdanov, 2002; Abubakar et al., 2004), we introduce a regularizing term linearly into the cost functional to be able to incorporate prior information on the model. We now assume that \mathcal{D} is discretized into N_p cells and arrange $\boldsymbol{\chi}$ into a $3 \times N_p$ element vector $\boldsymbol{\chi} = (\chi_h, \chi_h, \chi_v)^T$. The modified optimization problem becomes

$$\begin{aligned}
\underset{\mathcal{W}_{\text{mCSEM}}, \mathcal{W}_{\text{MT}}, \boldsymbol{\chi}}{\operatorname{argmin}} \quad & (F_1(\mathcal{W}_{\text{mCSEM}}, \mathcal{W}_{\text{MT}}, \boldsymbol{\chi}) + \lambda^2 F_2(\boldsymbol{\chi})) = \\
\underset{\mathcal{W}_{\text{mCSEM}}, \mathcal{W}_{\text{MT}}, \boldsymbol{\chi}}{\operatorname{argmin}} \quad & (F_1(\mathcal{W}_{\text{mCSEM}}, \mathcal{W}_{\text{MT}}, \boldsymbol{\chi}) + \lambda^2 \|\boldsymbol{\Omega}(\boldsymbol{\chi} - \boldsymbol{\chi}^{\text{ref}})\|_{\mathcal{D}}^2).
\end{aligned} \tag{29}$$

Here, F_2 allows including prior information concerning the model. Specifically, $\boldsymbol{\chi}^{\text{ref}}$ can represent a reference model, e.g., an expected solution; $\boldsymbol{\Omega}$ is some weighting matrix; and $\lambda \in \mathbb{R}$ is a weighting parameter controlling the trade-off between $F_1(\mathcal{W}_{\text{mCSEM}}, \mathcal{W}_{\text{MT}}, \boldsymbol{\chi})$ and $F_2(\boldsymbol{\chi})$. This parameter needs to be chosen appropriately to balance the terms properly.

We choose λ by inspection such that the term F_2 does not dominate the cost functional, and we relax it toward zero to not over-emphasize the regularizer. For more details on the minimization procedure and comments on the computational complexity, refer to Wiik et al. (2011).

Estimating the effective MT source

Due to the formulation in terms of the field components, we need to perform two main tasks: First we need to process frequency domain data on the field component form from the recorded time series and, second, estimate the effective incident plane wave corresponding to the data. The first task was performed by applying a fast Fourier transform to fixed-length subsequences of the total time series outside towing operations and avoiding obviously noisy data by inspection. Afterward, for each station, the mean of the output from several subsequences was calculated to form an average spectrum associated with acquired data and used as input to the inversion. We note that for this approach, we need to consider time segments overlapping at all receivers because the data all need to correspond to the same effective source. This is a drawback compared to impedances, where the source signature is removed when calculating the impedances. See Figure 2 for an illustration of the permitted time window for the receivers shown in the real data example.

The latter task was performed by means of a reference receiver deployed at a location where the response from the subsurface structures can be approximated by that of a 1D layered earth at the chosen frequencies and which contains no effects from nearby higher-dimensional structures such as, for example, salt diapirs. Under the 1D assumption, the two orthogonal source polarizations give rise to two orthogonal field polarizations that propagate independently. This allows us to separate the estimation of the two source polarizations. Figure 3 shows the processed results from the contractor at the reference receiver for the real data example considered later. The processing sequence started by eliminating particularly noisy sections of the recorded time series, before combining the methods described in Larsen et al. (1996) and Chave and Thomson (2004) to estimate the impedances. Remote referencing was applied due to the poorly recorded magnetic field. Figure 3 displays the typical 1D symmetries of the impedance tensor. The dimensionality parameter in Figure 3c is defined as the skew of the impedance tensor

$$\frac{|Z_{xx} + Z_{yy}|}{|Z_{xy} - Z_{yx}|}, \quad (30)$$

where Z_{ij} denotes the elements of the impedance tensor. Such a receiver is usually available because reference receivers are taken into account in survey planning. Further, a 1D model that fits the data was available from previous analysis.

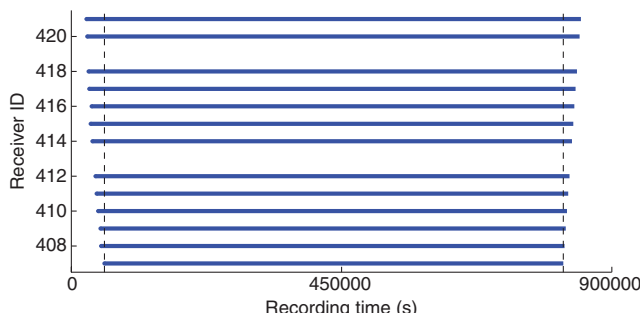


Figure 2. Recording times for each receiver. Allowed time window is between the black dashed lines.

Then, for each frequency and polarization, we consider the problem of solving Maxwell's equations in the 1D model at the reference receiver. In this setting, the measured field at the seabed is the solution in the 1D model due to the real effective source, for which we want to estimate the magnitude and phase. We then model a source with known magnitude and phase, and the same polarization. The field transmitted across the sea surface from these two sources differs only by a complex factor because the polarization is the same. Due to the linearity of Maxwell's equations, this factor is also the ratio between field components associated with the two sources, and this ratio can now be estimated using the receiver measurements.

NUMERICAL EXAMPLES

In this section, we present numerical results from three synthetic cases and one real case. In all cases, Ω is chosen as an approximation to the Laplacian operator acting on χ_h and χ_v independently, with different weights on horizontal and vertical smoothing. The vertical smoothing is set to one-third of the horizontal. The data weights in the examples are chosen as either 0 or 1, specified only to remove particularly noisy data points. Weighting schemes using the data error are preferred but not applied here due to reasons discussed in the Conclusions section. Five percent Gaussian noise is added to the scattered fields in the synthetic examples.

Anisotropic overburden

In the first test, we investigate the performance of joint inversion on a case with anisotropic overburden and compare it to the MT inversion results and mCSEM inversion using the MT result as the initial and prior model. We modeled a single inline mCSEM data line with a single frequency of 0.25 Hz and 53 equidistant source positions between -13,000 m and 13,000 m, and four MT frequencies at 0.1, 0.05, 0.025, and 0.01 Hz. The response was recorded at 17 receivers equidistantly spaced between -8000 m and 8000 m. In the inversion, we use the inline electric and crossline magnetic field components from the mCSEM data and the horizontal components of the electric field from the MT data. The domain \mathcal{D} is chosen to have cell size $\Delta x = \Delta y = 500$ m, while the vertical mesh has 18 cells with size increasing with depth from 50 m at the top to about 110 m at the bottom. The extent of domain \mathcal{D} is chosen as $-9000 \text{ m} \leq x \leq 9000 \text{ m}$, $-2000 \text{ m} \leq y \leq 2000 \text{ m}$, and $700 \text{ m} \leq z \leq 2000 \text{ m}$. The results are displayed as an intersection directly below the receiver line at $y = 0$ m because we only have one line of receivers. Figure 4 shows the true model, which contains a 500-m water column with conductivity of 3.2-S/m and a 1-S/m subsurface. An anisotropic layer is embedded in the subsurface with conductivity $\sigma_h = 2$ -S/m and anisotropy coefficient $Y = 4$, and a 0.02-S/m resistor is situated below. The true anomaly stretches 2 km both out of and into the plane displayed in the figure. The isotropic initial model used for MT and joint inversion is shown in Figure 5. For the mCSEM inversion, we used the horizontal conductivity obtained from MT inversion as initial model for σ_h , and the initial model described for the MT and joint inversion for σ_v . For the mCSEM inversion, the MT result was used as prior information; i.e., a nonzero χ^{ref} , in σ_h , while no prior was assigned to σ_v . This was done to include information from the MT inversion performed earlier into the mCSEM inversion. No priors were assigned in the MT and joint inversions; that is, $\chi^{\text{ref}} = 0$.

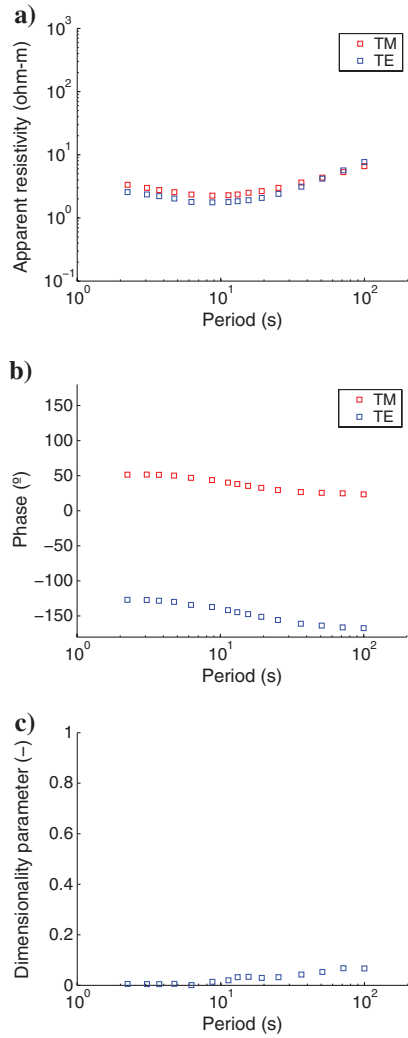


Figure 3. Processed data on impedance form from contractor. (a) Apparent resistivity, (b) phase, and (c) dimensionality parameter defined by equation 30.

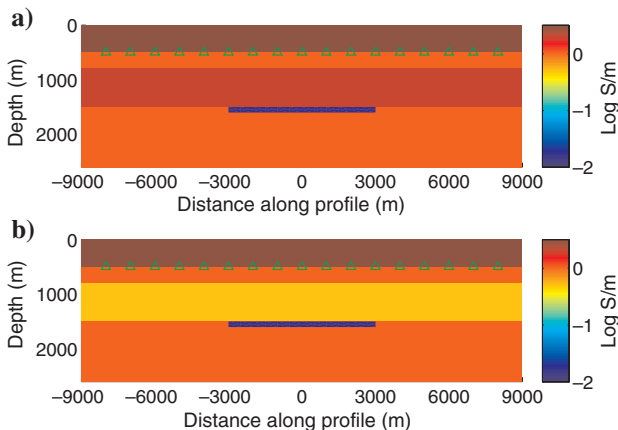


Figure 4. True model with anisotropic overburden: (a) σ_h and (b) σ_v .

The result from the pure MT inversion is shown in Figure 6. As expected, it is only sensitive to σ_h due to the vertically incident plane wave, and it does not sense the resistor below the anisotropic formation. Figure 7 shows the result from mCSEM inversion, where we have used the MT inversion result both as the prior and initial model. This procedure predicts anisotropy in the overburden, but the position of the formation is wrong and the estimated conductivities are wrong. However, it agrees with the existence of a resistor at approximately the correct depth, but it does not have the correct horizontal extent. The resistor appears only in the σ_v estimate because the anomalous currents in long, thin resistors are vertical.

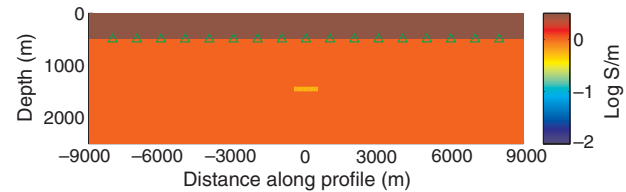


Figure 5. Isotropic initial model used in the example with anisotropic overburden.

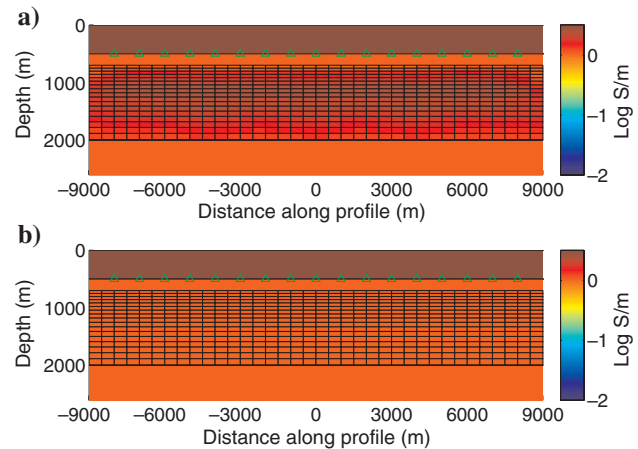


Figure 6. MT inversion result on the model with anisotropic overburden: (a) σ_h and (b) σ_v . The grid shows the inversion domain.

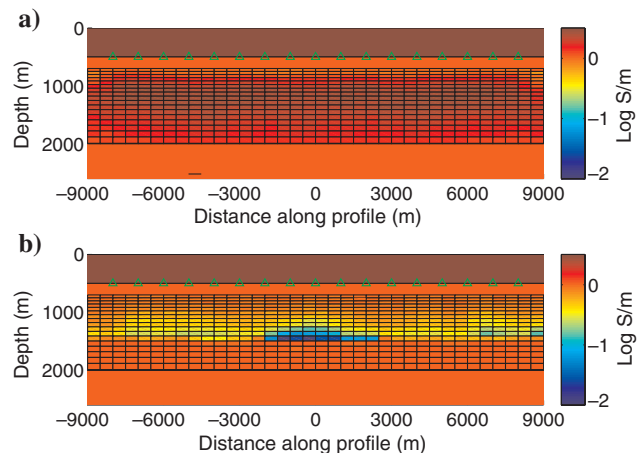


Figure 7. mCSEM inversion result on the model with anisotropic overburden: (a) σ_h and (b) σ_v . The grid shows the inversion domain.

Figure 8 shows the joint inversion results, and it also predicts the anisotropy in the overburden. However, it predicts a thicker formation compared to the sequential MT then mCSEM results. The conductivity estimates in this formation are similar in both the sequential MT then mCSEM and joint inversion. Further, the joint inversion also agrees with a resistor below the anisotropic structure in the same position as the sequential inversion, but with a slightly higher conductivity estimate. This is probably due to this structure being almost purely sensed by mCSEM data. The convergence histories for all three cases are shown in Figure 9, as an example of the convergence of the method.

From these results, it seems that similar results might be obtained by doing joint inversion or MT and mCSEM inversions sequentially. Thus, in such cases, the benefits of doing joint inversion may be limited if the sequential inversions are carried out properly. However, the joint inversion requires less human intervention and is more data controlled, and it is thus a useful tool for consistency checks between the data types.

Salt diapir example

In this example, we investigate the difference between doing sequential MT and mCSEM inversion versus joint inversion for a model describing a salt diapir. The experiment parameters are the same as in the previous example, and the true model is shown in Figure 10. The model is isotropic with salt conductivity set to 0.001 S/m, but the color scale is clipped at 0.01 S/m for better illustrations. The water column is 500-m deep with a conductivity of 3.2 S/m, and the subsurface has conductivity of 1 S/m. The domain \mathcal{D} is chosen to have cell size $\Delta x = \Delta y = 500$ m, while the vertical mesh has 26 cells with size increasing with depth from 50 m at the top to about 160 m at the bottom. The extent of the domain \mathcal{D} is chosen as $-6000 \text{ m} \leq x \leq 6000 \text{ m}$, $-2000 \text{ m} \leq y \leq 2000 \text{ m}$, and $600 \text{ m} \leq z \leq 3000 \text{ m}$. The initial model for MT and joint inversion is shown in Figure 11.

The results are shown in Figures 12–14. From Figure 12, we see that although the conductivity estimate is inaccurate, the MT inversion is able to approximately position the bottom of the salt structure. The width of the top structure is slightly too narrow. In the vertical conductivity, we observe some instability effects that could

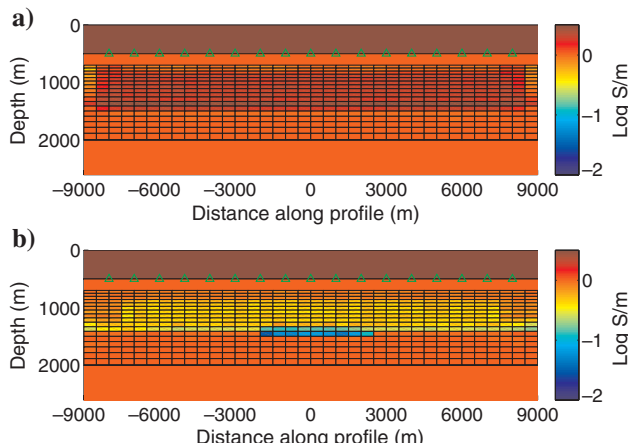


Figure 8. Joint mCSEM and MT inversion result on the model with anisotropic overburden: (a) σ_h and (b) σ_v . The grid shows the inversion domain.

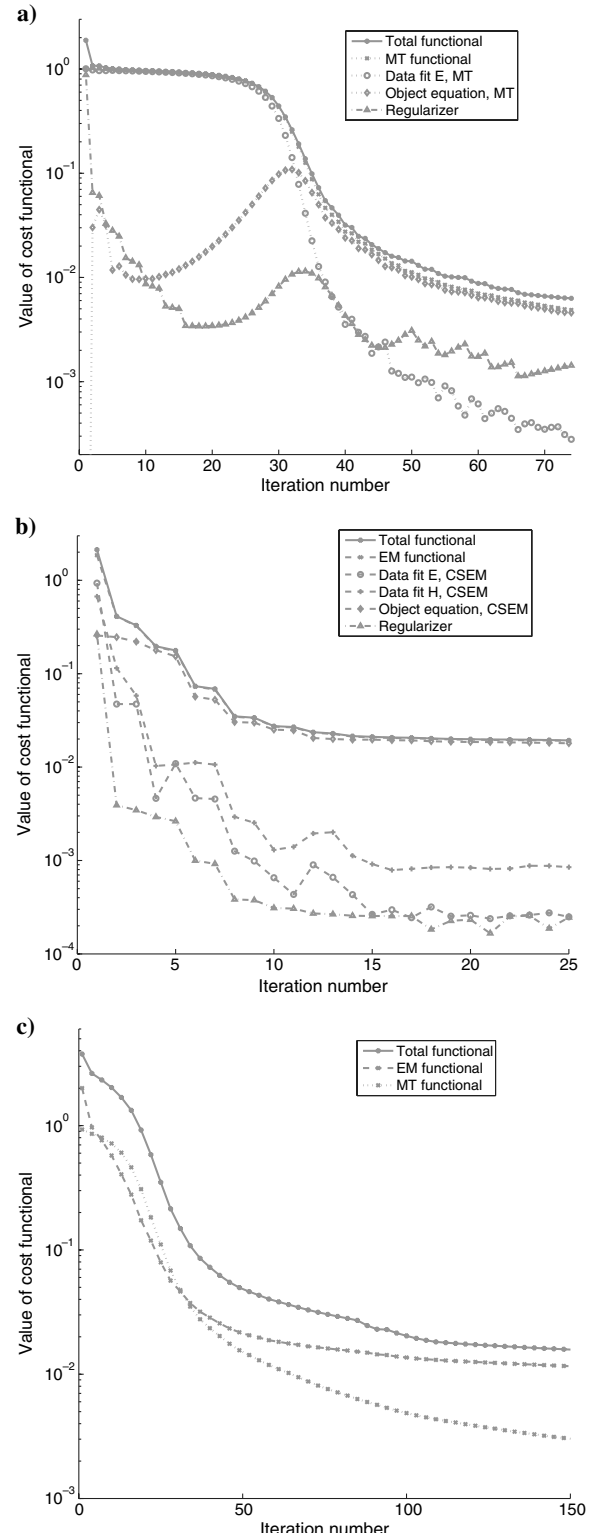


Figure 9. Cost functionals for cases in example with anisotropic overburden: (a) MT, (b) mCSEM, and (c) joint. Legend explanation: cost functional, equation 29; mCSEM functional, first three terms in equation 22; data fit E-field mCSEM, first term in equation 22; data fit H-field mCSEM, second term in equation 22; object equation mCSEM, third term in equation 22; MT functional, last three terms in equation 22; data fit E-field MT, fourth term in equation 22; object equation MT, sixth term in equation 22; regularizer, last term of equation 29.

be due to regularization or noisy data at the top. Figure 13 was then produced by using the MT result as the initial model and prior information in the mCSEM inversion in the same way as in the previous example. The sequential MT then mCSEM inversion in Figure 13 shows that it is not able to determine the correct location of the bottom of the structure. This is due to the frequency content of the mCSEM data. The joint inversion result in Figure 14, however, predicts a larger contrast, and is able to place the bottom salt at approximately the correct depth. It does not predict a thin neck, as the MT inversion did, but rather a big structure with a slightly decreasing width until the bottom. Further, the joint inversion also predicts the top of the salt structure to be wider. This could imply that for imaging salt structures, joint inversion is preferred over sequential MT and mCSEM inversion in some situations, and that MT data are helpful to image the lower parts. Increasing the frequency band will probably also aid the inversion.

The reason for the salt structure being best visible in the horizontal conductivity for all inversions is probably due to the predominantly horizontal currents in the MT signal. The mCSEM signal induces both horizontal and vertical currents, and the inversions involving mCSEM

data thus also show some resistivity in the shallow part of the salt in the vertical conductivity. However, because we started the mCSEM inversion with the MT result, this anomaly is not as clear as the one in the horizontal conductivity. To investigate the difference between the anisotropic and isotropic inversion on this isotropic model, we conducted an isotropic joint inversion with the same parameters. The result from this inversion is shown in Figure 15, which does not differ much from the horizontal conductivity result in Figure 14.

Hydrocarbons near a salt diapir

In this example, we consider a hydrocarbon reservoir near a salt structure. The experimental parameters are very similar to the ones of the previous examples, and the true model is shown in Figure 16. The hydrocarbon conductivity is set to 0.1 S/m, and the other model conductivities and cell sizes are the same as in the previous example. The extent of the domain \mathcal{D} is chosen as $-9000 \text{ m} \leq x \leq 9000 \text{ m}$, $-2000 \text{ m} \leq y \leq 2000 \text{ m}$, and $600 \text{ m} \leq z \leq 3000 \text{ m}$. The initial model for MT and joint inversion is shown in Figure 17. The mCSEM inversion start and prior models were set as in the previous examples.

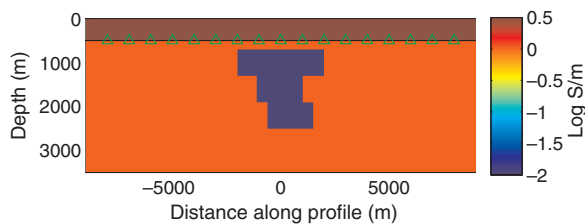


Figure 10. Isotropic salt diapir model.

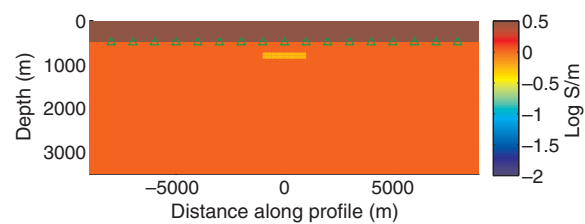


Figure 11. Initial model in salt diapir example.

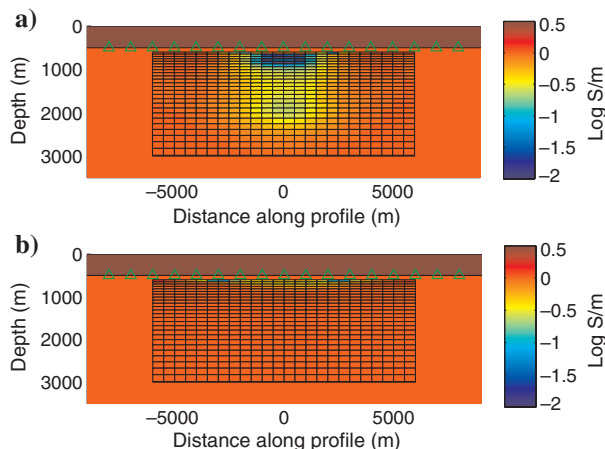


Figure 12. MT inversion result on the salt diapir model: (a) σ_h and (b) σ_v . The grid shows the inversion domain.

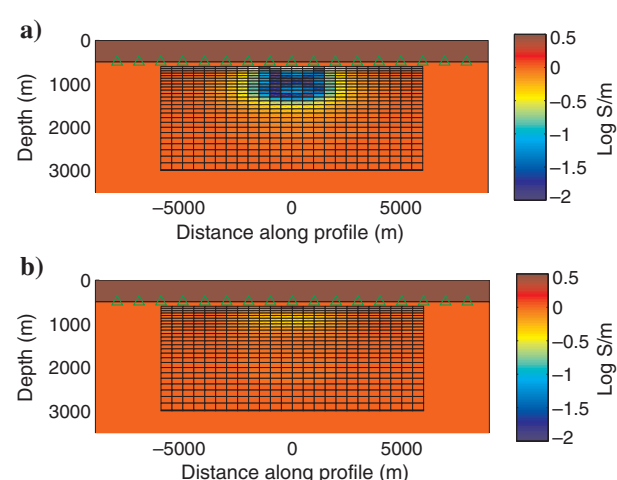


Figure 13. mCSEM inversion result on the salt diapir model: (a) σ_h and (b) σ_v . The grid shows the inversion domain.

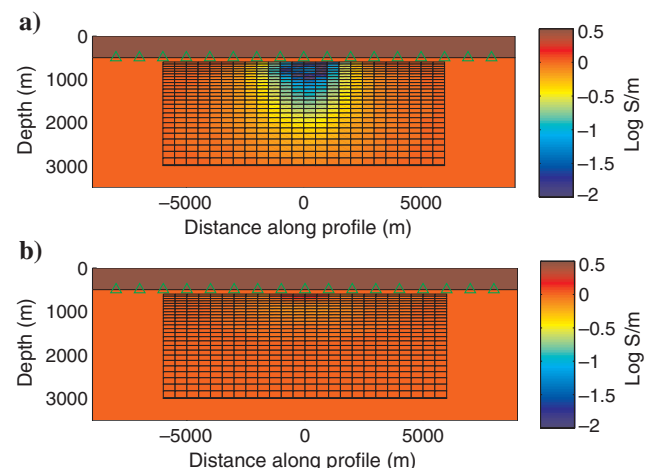


Figure 14. Joint mCSEM and MT inversion result on the salt diapir model: (a) σ_h and (b) σ_v . The grid shows the inversion domain.

From Figures 18–20, we observe similar trends as in the previous example. However, the hydrocarbon reservoir is not visible in any of the inversion results, and even the salt body is worse recovered. Using both the sequential and joint strategy, a nearly invisible resistive imprint is present with the approximate horizontal extent of

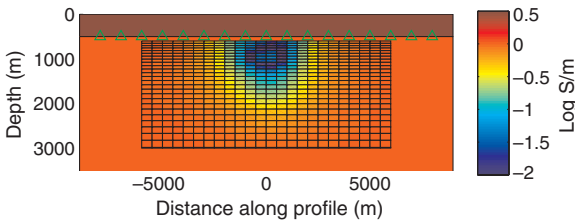


Figure 15. Isotropic joint mCSEM and MT inversion result on salt diapir model. The grid shows the inversion domain.

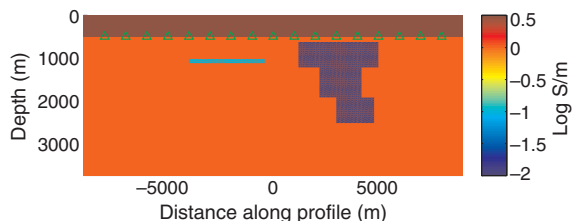


Figure 16. Isotropic model of reservoir near salt diapir.

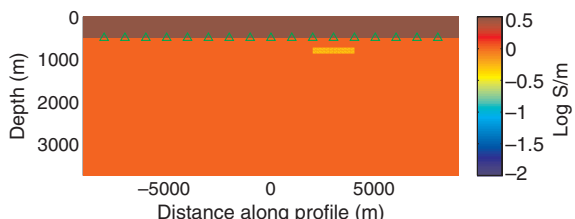


Figure 17. Initial model in example with a reservoir near a salt diapir.

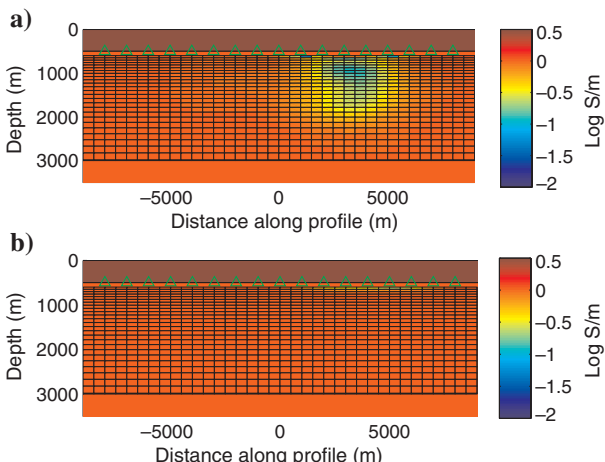


Figure 18. MT inversion result on reservoir near the salt diapir: (a) σ_h and (b) σ_v . The grid shows the inversion domain.

the reservoir in the vertical conductivity, but no resistive body is introduced. This exemplifies the difficulties of EM inversion with respect to hydrocarbons near large, highly resistive structures, which is a known challenge from, e.g., the Barents Sea. As seen from the data in Figure 21, the anomaly connected to the salt diapir is much larger than that connected to the reservoir. It probably works as an attractor in the optimization procedure because simply fitting this anomaly will lead to a high degree of data fit measured in the L2 norm and traps the algorithm in a local minimum. In Figure 22, we show the joint inversion result with the reservoir present in the initial model. In this case, it is not completely removed, but remains in the model heavily smoothed. This inversion also terminated with a slightly better data fit compared to the joint inversion without the reservoir present in the initial model. The problem is thus extremely sensitive to the initial model. A possible solution to this problem is to include the salt diapir in the background model, as described by Zhdanov et al. (2007), assuming it is well described after an initial inversion. This may mitigate

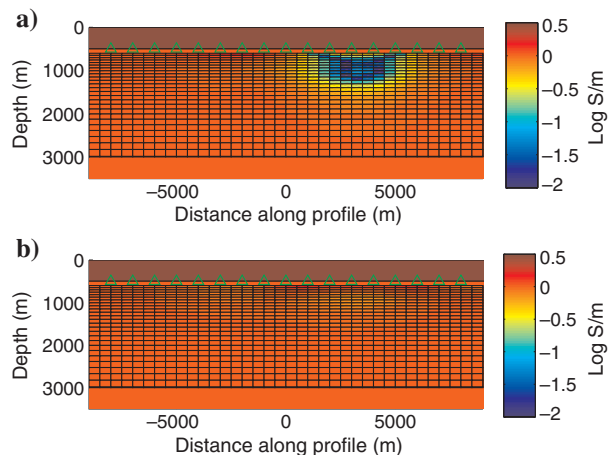


Figure 19. mCSEM inversion result on reservoir near the salt diapir: (a) σ_h and (b) σ_v . The grid shows the inversion domain.

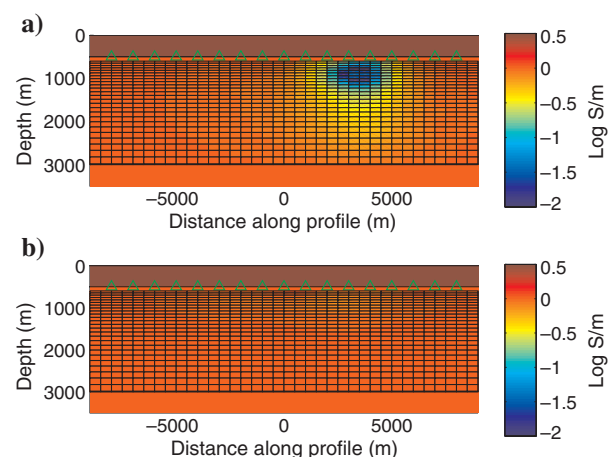


Figure 20. Joint mCSEM and MT inversion result on the reservoir near the salt diapir: (a) σ_h and (b) σ_v . The grid shows the inversion domain.

the attractor associated with the salt diapir by including it in the background field.

Example from the Barents Sea

Here, we show an example of salt imaging in the Barents Sea using electromagnetic data. Earlier work has been published from the same area (Hokstad et al., 2011; Ceci et al., 2012). The salt is of the Permian age, and the main stages of diapirism took place in the Triassic. The salt was reactivated in the Paleogene. The subsequent erosion in Late Paleogene removed more than 1000 m of Cretaceous and younger sediments. At present, the top of the diapirs is separated from the sea floor only by a thin Quarternary layer. The hydrocarbon play is mainly salt-related traps in eustaurine sandstones of Carnian age.

Seismic imaging in the vicinity of the salt diapirs is very difficult, due to weak primaries, strong multiples, and diffraction noise. The salt structures are surrounded by a seismic “shadow zone” where interpretation of continuous seismic reflectors is difficult. However,

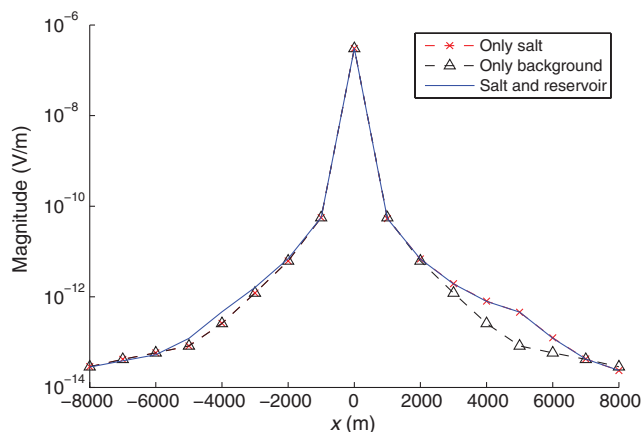


Figure 21. Inline electric field amplitude recorded with the source placed between the salt diapir and the reservoir for different models in the example with a hydrocarbon reservoir near salt.

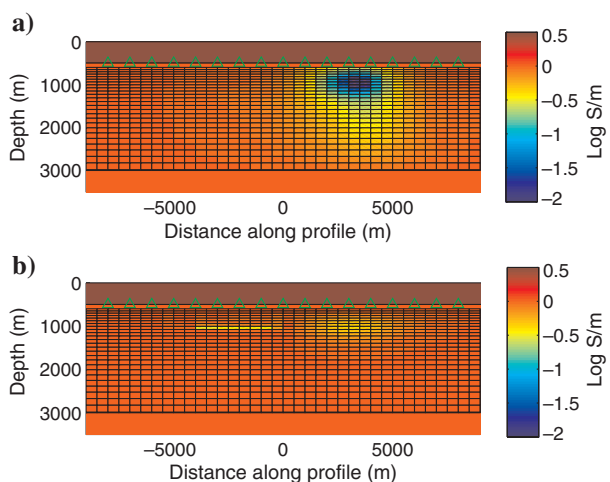


Figure 22. Joint mCSEM and MT inversion result on the reservoir near the salt diapir with reservoir present in initial model: (a) σ_h and (b) σ_v . The grid shows the inversion domain.

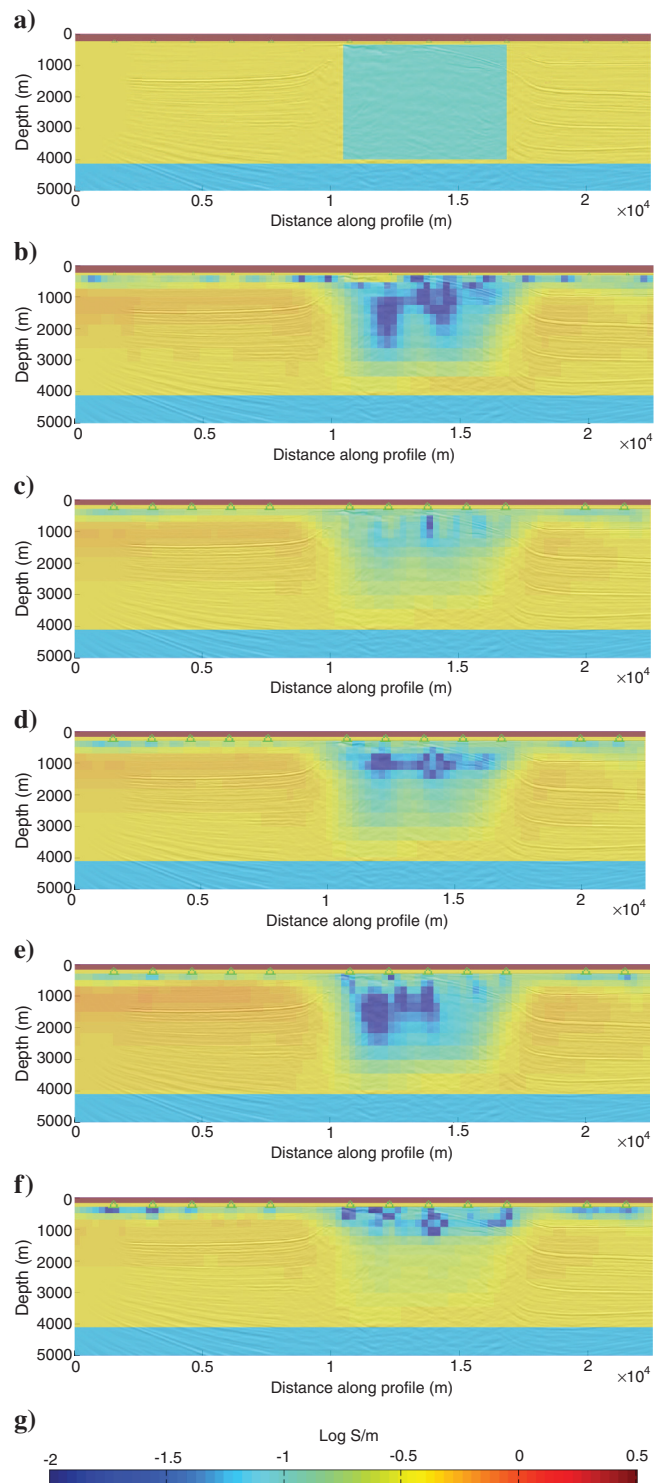


Figure 23. Inversion results performing MT, sequential MT, and mCSEM inversion and simultaneous joint inversion on a real data example. (a) Isotropic initial model used for MT and joint inversions, (b) MT inversion result, (c) horizontal conductivity, mCSEM inversion using MT result as the reference and initial model, (d) vertical conductivity, mCSEM inversion using MT result as reference and initial model, (e) horizontal conductivity, joint inversion, (f) vertical conductivity, joint inversion, and (g) color bar for inversion results on real data.

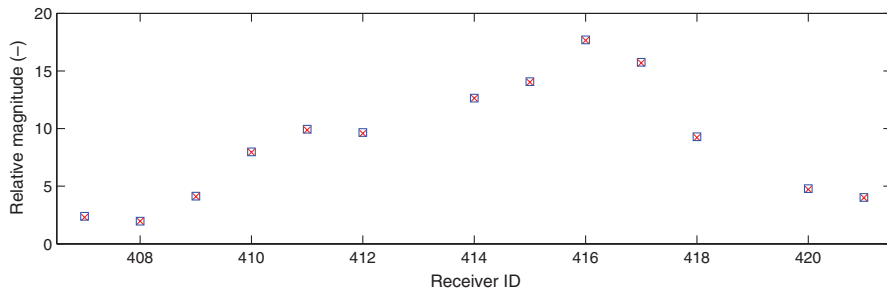


Figure 24. Scattered field for MT inversion at 0.01 Hz for e_x , normalized against the scattered field at receiver close to the reference receiver. Red stars denote input data, and blue squares denote synthetic response.

in the Uranus well (7227/11-1), salt resistivity of 1000 ohm-m and more was logged. This suggests that electromagnetic methods may be useful for delineating the salt size and shape. In 2007, mCSEM and MT data were recorded over several salt diapirs in the area.

The data considered consists of 17 receivers along a line. For the mCSEM data used here, we used an inline electric field component at a single frequency (0.508 Hz) and an inline and crossline electric field at four frequencies in the range 0.01–0.5 Hz for the MT inversion. The MT data were processed using 24 h of listening time, and the frequencies lie in the range specified by the contractor to have sufficiently strong signal for MT purposes. We did not use magnetic fields for the MT data because the recorded magnetic fields often are of lower quality than the electric data. For the MT and joint inversions, we used a zero reference model in the regularization term and the initial model given in Figure 23a, while for the mCSEM inversion, the MT result was used both as the initial and reference model in both horizontal and vertical conductivity. The figures display the results from receiver ID 7 to receiver ID 21 because this is the relevant area concerning the salt diapir. The MT inversion was performed using isotropic inversion, while mCSEM and joint inversions were run with TIV anisotropy. For each receiver, we considered 51 source positions. The domain \mathcal{D} was chosen as $-1000 \text{ m} \leq x \leq 31000 \text{ m}$, $-2000 \text{ m} \leq y \leq 2000 \text{ m}$, $330 \text{ m} \leq z \leq 4000 \text{ m}$, with $\Delta x = 250 \text{ m}$, $\Delta y = 500 \text{ m}$ and a vertical mesh size that increased with depth. An example of the input MT data is shown in Figure 24, together with the synthetic MT data from the MT inversion result. It shows the scattered field in e_x normalized against the scattered field at a receiver close to the reference. We observe the increase in amplitude at receivers 14–17, which corresponds to the salt diapir.

From Figure 23b and 23g, we see that all the inversion results place a resistive body that extends to a depth between 3000 and 3500 m and at the correct lateral position compared to the seismic image in the background. We observe that in the sequential inversion, the result following the mCSEM inversion shown in Figure 23c and 23d places more vertical resistivity than horizontal resistivity in the most shallow part of the diapir. This may be a regularization effect, caused by using the MT result as reference model in both horizontal and vertical conductivity. The joint inversion results, shown in Figure 23e and 23f, show that without any prior information, both MT and mCSEM data support having most horizontal resistivity. However, all inversions predict approximately the same thickness of salt. The rms misfit for the MT data is 10% for both the stand-alone MT inversion and the joint inversion, while for the mCSEM data, the misfit increases from 7% to 7.4% from the mCSEM to the joint inversion.

CONCLUSIONS

We have presented an anisotropic joint inversion method for mCSEM and MT data based on a scattered field formulation. The method was used for synthetic studies concerning the benefits of doing joint inversion compared to sequential MT then mCSEM inversion. We found that for anisotropic layers in the overburden, the two strategies may produce similar results, while the synthetic examples show that for imaging large salt structures, joint inversion could be a useful tool. Due to the MT data, joint mCSEM/MT inversion can be used to determine a possible bottom of a salt diapir, and due to the mCSEM data, a better conductivity estimate and a more accurate lateral extension of the top is produced. Furthermore, we demonstrated the difficulties in EM inversion for hydrocarbon prospecting near large, highly resistive structures, such as salt. This situation probably requires very good initial models because the salt response dominates the recorded signal. The benefits of joint inversion could be different in more complex media, compared to the simple models considered here for principal studies.

Finally, we considered a real data example from the Nordkapp basin, where we applied the algorithm to image a salt diapir. The example shows that it is possible to apply this method, which is based on field components rather than impedances, to real data. The procedure used is dependent on a reference receiver to estimate the incident plane wave, which may introduce artifacts into the inversion if not properly accounted for. We note that the result of performing a joint inversion is not very different from performing sequential MT then mCSEM inversions, using the MT result as initial model and prior information in the inversion for mCSEM inversion, in this case.

However, joint inversion constitutes a very useful tool for checking data consistency with respect to inversion and interpretation results obtained from stand-alone or sequential use of other methods. Further, it requires less intermediate interpretation or processing to determine for instance proper regularization levels, and it is thus more data controlled. Joint inversion may not be absolutely necessary in all situations, but it is always useful in terms of consistency checks.

An important effect to assess in further studies are the uncertainties associated with errors in the source estimation procedure. For the source estimation approach suggested here, the error can be split into two parts. The first part is due to choosing a wrong 1D model at the reference receiver, which will give a global relative shift in the estimated plane wave source. The second part, which is due to choosing a 1D model although the response may be higher dimensional, is more difficult to analyze. The effect of this error in the estimated source field, and the subsequent inversion results, will

be case dependent and may vary across a single survey, and if it is deemed significant, a different strategy to the source estimation challenge is needed. Further, to improve the inversion results, a weighting scheme based on errors in the input data is desirable. This was not applied here because errors for the mCSEM data were not processed in the field data example. Further, how to estimate these for MT data on the field component form is an open question, which needs to be studied. It cannot be done in the same way as for mCSEM data, by studying the power spectrum between source frequencies, due to the more continuous nature of the frequency band for MT data. Also, they are not the same as for MT impedances.

ACKNOWLEDGMENTS

T. Wiik acknowledges Statoil ASA for sponsoring his Ph.D. project. B. Ursin has received financial support from VISTA and from the Norwegian Research Council through the ROSE project. We thank GdF Suez and Statoil for permission to publish the real data example. We also thank the reviewers, A. Ray, B. Heincke, and one anonymous, for the constructive criticism we received, which greatly improved this paper.

REFERENCES

- Abubakar, A., T. M. Habashy, V. L. Druskin, L. Knizhnerman, and D. Alumbaugh, 2008a, 2.5D forward and inverse modeling for interpreting low-frequency electromagnetic measurements: *Geophysics*, **73**, no. 4, F165–F177, doi: [10.1190/1.2937466](https://doi.org/10.1190/1.2937466).
- Abubakar, A., W. Hu, P. M. van den Berg, and T. M. Habashy, 2008b, A finite-difference contrast source inversion method: *Inverse Problems*, **24**, 065004, doi: [10.1088/0266-5611/24/6/065004](https://doi.org/10.1088/0266-5611/24/6/065004).
- Abubakar, A., M. Li, J. Liu, and T. Habashy, 2009, Simultaneous joint inversion of MT and CSEM data using a multiplicative cost function: 79th Annual International Meeting, SEG, Expanded Abstracts, 719–723.
- Abubakar, A., and P. M. van den Berg, 2004, Iterative forward and inverse algorithms based on domain integral equations for three-dimensional electric and magnetic objects: *Journal of Computational Physics*, **195**, 236–262, doi: [10.1016/j.jcp.2003.10.009](https://doi.org/10.1016/j.jcp.2003.10.009).
- Abubakar, A., P. M. van den Berg, and J. J. Mallorqui, 2002, Imaging of biomedical data using a multiplicative regularized contrast source inversion method: *IEEE Transactions on Microwave Theory and Techniques*, **50**, 1761–1771, doi: [10.1109/TMTT.2002.800427](https://doi.org/10.1109/TMTT.2002.800427).
- Abubakar, A., P. M. van den Berg, and S. Y. Semenov, 2004, A robust iterative method for Born inversion: *IEEE Transactions on Geoscience and Remote Sensing*, **42**, 342–354, doi: [10.1109/TGRS.2003.821062](https://doi.org/10.1109/TGRS.2003.821062).
- Ceci, F., A. Lovatini, L. Masnaghetti, K. Hokstad, and V. Antonsdottir, 2012, Multi measurement imaging using seismic CSEM MMT and FTG data for salt dome evaluation in the Nordkapp Basin: 74th Annual International Conference and Exhibition, EAGE, Extended Abstracts, B034.
- Chave, A., and D. Thomson, 2004, Bounded influence magnetotelluric response function estimation: *Geophysical Journal International*, **157**, 988–1006, doi: [10.1111/j.1365-246X.2004.02203.x](https://doi.org/10.1111/j.1365-246X.2004.02203.x).
- Colombo, D., T. Keho, E. Janoubi, and W. Soyer, 2011, Sub-basalt imaging with broadband magnetotellurics in NW Saudi Arabia: 81st Annual International Meeting, SEG, Expanded Abstracts, 619–623.
- Colton, D., and R. Kress, 1992, Inverse acoustic and electromagnetic inverse scattering theory: Springer Verlag.
- Commer, M., and G. Newman, 2009, Three-dimensional controlled-source electromagnetic and magnetotelluric inversion: *Geophysical Journal International*, **178**, 1305–1316, doi: [10.1111/j.1365-246X.2009.04216.x](https://doi.org/10.1111/j.1365-246X.2009.04216.x).
- Constable, S. C., R. L. Parker, and C. G. Constable, 1987, Occam's inversion: A practical algorithm for generating smooth models from electromagnetic sounding data: *Geophysics*, **52**, 289–300, doi: [10.1190/1.1442303](https://doi.org/10.1190/1.1442303).
- de Hoop, A. T., 1995, Handbook of radiation and scattering of waves: Academic Press.
- Eidesmo, T., S. Ellingsrud, L. M. MacGregor, S. Constable, M. C. Sinha, S. Johansen, F. N. Kong, and H. Westerdahl, 2002, Sea bed logging (SBL), a new method for remote and direct identification of hydrocarbon filled layers in deepwater areas: *First Break*, **20**, 144–152.
- Fox, L., and O. Ingerov, 2007, Natural source EM for offshore hydrocarbon detection offers potential cost savings: *First Break*, **25**, 87–94.
- Green, G., 1828, An essay on the application of mathematical analysis to the theories of electricity and magnetism: T. Wheelhouse.
- Heincke, B., M. Jegen, and R. Hobbs, 2006, Joint inversion of MT, gravity and seismic data applied to sub-basalt imaging: 76th Annual International Meeting, SEG, Expanded Abstracts, 784–789.
- Hohmann, G. W., 1987, Numerical modeling for electromagnetic methods of geophysics, in Nabighian, M. N., ed., *Electromagnetic methods in applied geophysics*: Volume 1: Theory: SEG, 31–363.
- Hokstad, K., B. Fotland, G. Mackenzie, V. Antonsdottir, S.-K. Foss, C. Stadtler, C. Fichler, M. Haverl, B. M. T. Waagan, E. A. Myrland, L. Masnaghetti, F. Ceci, and P.-Y. Raya, 2011, Joint imaging of geophysical data: Case history from the Nordkapp Basin, Barents Sea: 81st Annual International Meeting, SEG, Expanded Abstracts, 1098–1102.
- Jegen, M., R. Hobbs, P. Tarits, and A. Chave, 2009, Joint inversion of marine magnetotelluric and gravity data incorporating seismic constraints: Preliminary results of sub-basalt imaging off the Faroe Shelf: *Earth and Planetary Science Letters*, **282**, 47–55, doi: [10.1016/j.epsl.2009.02.018](https://doi.org/10.1016/j.epsl.2009.02.018).
- Larsen, J., R. Mackie, A. Manzella, A. Fordelisi, and S. Rieven, 1996, Robust smooth magnetotelluric transfer functions: *Geophysical Journal International*, **124**, 801–819, doi: [10.1111/j.1365-246X.1996.tb05639.x](https://doi.org/10.1111/j.1365-246X.1996.tb05639.x).
- Mackie, R., D. M. Watts, and W. Rodi, 2007, Joint 3D inversion of marine CSEM and MT data: 77th Annual International Meeting, SEG, Expanded Abstracts, 574–578.
- McOwen, R., 1996, Partial differential equations. Methods and applications: Prentice-Hall.
- Negi, J. G., and P. D. Saraf, 1989, Anisotropy in geoelectromagnetism: Elsevier.
- Newman, G. A., M. Commer, and J. J. Carazzone, 2010, Imaging CSEM data in the presence of electrical anisotropy: *Geophysics*, **75**, no. 2, F51–F61, doi: [10.1190/1.3295883](https://doi.org/10.1190/1.3295883).
- Newman, G. A., and G. M. Hoversten, 2000, Solution strategies for two- and three-dimensional electromagnetic inverse problems: *Inverse Problems*, **16**, 1357–1375, doi: [10.1088/0266-5611/16/5/314](https://doi.org/10.1088/0266-5611/16/5/314).
- Plessix, R.-E., and W. A. Mulder, 2008, Resistivity imaging with controlled-source electromagnetic data: Depth and data weighting: *Inverse Problems*, **24**, 034012, doi: [10.1088/0266-5611/24/3/034012](https://doi.org/10.1088/0266-5611/24/3/034012).
- Price, A., and D. Watts, 2009, Vertical and horizontal resolution considerations for a joint 3D CSEM and MT inversion: 79th Annual International Meeting, SEG, Expanded Abstracts, 699–703.
- Rodi, W., and R. L. Mackie, 2001, Nonlinear conjugate gradients algorithm for 2-D magnetotelluric inversion: *Geophysics*, **66**, 174–187, doi: [10.1190/1.1444893](https://doi.org/10.1190/1.1444893).
- Sasaki, Y., 2013, Three-dimensional inversion of marine CSEM and MT data: An approach to shallow-water problem: *Geophysics*, **78**, no. 1, E59–E65, doi: [10.1190/geo2012-0094.1](https://doi.org/10.1190/geo2012-0094.1).
- Simpson, F., and K. Bahr, 2005, Practical magnetotellurics: Cambridge University Press.
- Tikhonov, A. N., and V. Y. Arsenin, 1977, Solution of ill-posed problems: W. H. Winston and Sons.
- Wannamaker, P. E., G. W. Hohmann, and W. A. SanFilipo, 1984, Electromagnetic modelling of three-dimensional bodies in layered earths using integral equations: *Geophysics*, **49**, 60–74, doi: [10.1190/1.1441562](https://doi.org/10.1190/1.1441562).
- Wiik, T., L. Løseth, B. Ursin, and K. Hokstad, 2011, TIV contrast source inversion of CSEM data: *Geophysics*, **76**, no. 1, F65–F76, doi: [10.1190/1.3524270](https://doi.org/10.1190/1.3524270).
- Zhdanov, M., A. Gribenko, and M. Cuma, 2007, Regularized focusing inversion of marine CSEM data using minimum vertical-support stabilizer: 77th Annual International Meeting, SEG, Expanded Abstracts, 579–583.
- Zhdanov, M., L. Wan, A. Gribenko, M. Cuma, K. Key, and C. G. Constable, 2009, Rigorous 3D inversion of marine magnetotelluric data in the area with complex bathymetry: 79th Annual International Meeting, SEG, Expanded Abstracts, 729–733.
- Zhdanov, M. S., 2002, *Geophysical inverse theory and regularization problems*: Elsevier.